Journal of the European Ceramic Society 45 (2025) 117062

Contents lists available at ScienceDirect

Journal of the European Ceramic Society

journal homepage: www.elsevier.com/locate/jeurceramsoc

High-temperature annealing of calcium lanthanum sulfide

Alexandros Kostogiannes [a], Nicholas G. Rudawski [b], Brianna Ellsworth [a], Andrew Howe [c], Brian Butkus [a], Andrew Cooper [d], Kathleen A. Richardson [a,c], Romain Gaume [a,c,e,*], Parag Banerjee [a,e,f,g,*]

[a] Department of Materials Science & Engineering, University of Central Florida, Orlando, FL 32816, USA
[b] Herbert Wertheim College of Engineering, Nanoscale Research Facility, University of Florida, Gainesville, FL 32611, USA
[c] College of Optics and Photonics, CREOL, University of Central Florida, Orlando, FL 32816, USA
[d] Department of Mechanical and Aerospace Engineering, University of Central Florida, Orlando, FL 32816, USA
[e] NanoScience Technology Center, University of Central Florida, Orlando, FL 32816, USA
[f] REACT Faculty Cluster Initiative, University of Central Florida, Orlando, FL 32816, USA
[g] Florida Solar Energy Center, University of Central Florida, Orlando, FL 32816, USA

ARTICLE INFO

Keywords:
Calcium lanthanum sulfide
Thermal annealing
Aberration corrected scanning/transmission electron microscopy
Lanthanum oxysulfides

ABSTRACT

Calcium lanthanum sulfide ceramic with a target at% composition of CaS: La_2S_3 of 10 : 90 was subjected to annealing at 1100 °C in dry nitrogen ambient. Cross-sectional scanning/transmission electron microscopy was used to understand the changes to the stoichiometry and structure of the ceramic. It was found that residual, 'dissolved' oxygen (up to 5.4 at%) in the annealed sample diffused outwards while sulfur was lost to the ambient and calcium diffused inwards. These diffusion processes were accompanied by the formation of a sub-μm thick surface layer of La_2O_2S and a sub-surface layer of $La_{20}OS_{29}$ in the calcium-free zones. The phase formation of the oxysulfides was explained within the context of existing phase diagrams of La-O-S and Ca-La-S. Reaction modeling of the diffusion processes were used to explain the sequential mechanistic steps responsible for the formation of the oxysulfides on calcium lanthanum sulfide surfaces upon annealing.

1. Introduction

Calcium lanthanum sulfides (CLS) form an important class of ceramics that demonstrate long wave infrared (LWIR) transparency together with superior mechanical properties [1–5]. Previous work regarding CLS focused on the composition $CaLa_2S_4$ where, the CaS:La_2S_3 mole fraction is 50:50 with the compound crystallizing in the cubic-Th_3P_4 crystal structure [6,7]. It is known that a complete solid solution exists between $CaLa_2S_4$ and La_2S_3 [8]. It is thus possible to obtain various ratios of Ca: La in CLS with the cubic-Th_3P_4 crystal structure intact, compensated by the presence of cation vacancies [9–12]. Since the early 1980s several key material issues have emerged as technological bottlenecks in CLS ceramics, the most important being, i) thermal instability which is governed by sulfur volatilization during sintering and, ii) the presence of oxygen as a contaminant [8,13].

CLS is prone to oxidation resulting in the formation of secondary phases [14]. The secondary phases in turn cause optical scattering and absorption [8,15–18]. Indeed, optical absorption detrimental to transparency in the relevant mid- to LWIR spectral region, have been reported in CLS [8,19–21]. Specifically, the infrared (IR) bands at 9.2 μm and 11.0 μm were assigned to sulfates and sulfites, respectively. This fact was recently brought into question, especially for lanthanum-rich CLS ceramics [22]. Thus, for continued advancement in achieving oxygen-free CLS for superior mid- to LWIR transparency, it is imperative to understand oxygen's role within the crystal structure.

To this end, there are reports involving reactions in both open and closed environments to establish phase diagrams pertaining to the La-O-S and La-Ca-S systems [8,14,15,23]. For example, Kitazawa *et al.*,[23] reacted crystalline sulfur with various compounds (*e.g.*, β-La_2S_3, $La_2O_2SO_4$, LaS_2, La_2O_2S, and $La_2O_2S_2$) prepared in sealed ampoules maintained at 800 °C for two weeks and then quenched to 0 °C. The resulting phase diagram shows a complex interaction between La, O and S and points to the affinity of oxygen towards La_2S_3 resulting in the formation of a series of oxysulfides. Specific to CLS, Chess *et. al.*, reacted $CaCO_3$ and La_2O_3 under H_2S at temperatures of 950 – 1400 °C and generated a phase diagram between CaS and La_2S_3 [8]. The $CaLa_2S_4$

* Corresponding authors at: Department of Materials Science & Engineering, University of Central Florida, Orlando, FL 32816, USA.
E-mail addresses: gaume@ucf.edu (R. Gaume), parag.banerjee@ucf.edu (P. Banerjee).

https://doi.org/10.1016/j.jeurceramsoc.2024.117062
Received 25 July 2024; Received in revised form 4 November 2024; Accepted 6 November 2024
Available online 13 November 2024
0955-2219/© 2024 Elsevier Ltd. All rights are reserved, including those for text and data mining, AI training, and similar technologies.

forms a solid solution with La_2S_3 while maintaining the cubic-Th_3P_4 crystal structure. Even though calcium is critical for maintaining the stability of the cubic-Th_3P_4 crystal structure, it is possible that lanthanum-rich CLS can be stabilized in the presence of cation vacancies. However, no elaboration is made upon the interactions between the residual oxygen and the optical performance of the ceramics generated. Taken together, these results indicate that while there are known secondary phases of oxysulfides, limited information regarding the interaction of these phases with CLS is available. More importantly, the mechanistic steps that establish phase relationships between the La-O-S and La-Ca-S systems remain unknown.

Recently, our group published a study proposing that phase pure CLS can incorporate 'dissolved' oxygen within the lattice at multiple defect sites [24]. The dissolved oxygen can inhibit the optical performance in the mid- to LWIR spectral region. It was further shown that phase pure CLS ceramics produced from powders prepared *via* different synthesis routes contain nearly identical oxygen concentrations while demonstrating different optical characteristics. The resulting optical absorption bands appear at varying wavelengths and with varying intensities that cannot be merely attributed to the previously suggested impurities (*i.e.*, sulfates and sulfites) but are more likely caused by dissolved oxygen interacting with the CLS lattice. The above evidence provides a key link between dissolved oxygen in CLS and potential strategies by which its presence can be amplified to study the subtle structure and phase relationships in the La-Ca-S-O system.

Therefore, in this paper, and as a continuation of our efforts to understand the role of oxygen in CLS, the effect of high temperature (1100 °C) inert gas annealing on CLS was studied using scanning/transmission electron microscopy (S/TEM). The CLS ceramic used in the experiments is CaS: La_2S_3 10:90 (at%) with a Ca: La: S theoretical composition of 2.1: 38.3: 59.6 at%. This calcium-lean sample is well suited to study dissolved oxygen in CLS, as it contains a maximum of 9.5 at% lanthanum vacancies which may play an important role in determining the CLS phase stability and influence diffusion of various species in CLS. Further, the use of an inert gas for annealing excludes any extrinsic effects from oxygen in the ambient. Lastly, we note that S/TEM provides a powerful characterization tool to study phase transformations in CLS by providing compositional (*i.e.*, stoichiometry) and structural (*i.e.,* phase and crystallographic) information with μm- to pm-scale resolution. Our results establish stoichiometry, phase and crystallographic relationships under inert gas annealing conditions for CLS ceramics in the presence of dissolved oxygen.

2. Experimental

2.1. Ceramic preparation and annealing

CLS ceramics were prepared *via* hot pressing as described elsewhere [24]. The hot-pressed coupons were subsequently annealed using an OxyGon® hot-press furnace that was operated without applying any load. The furnace was equipped with graphite heating elements, insulation, and pressing rams that were encased within a molybdenum heat shield, all residing within a stainless-steel chamber. The samples were placed in an alumina crucible with a lid placed over top to prevent carbon contamination and loaded into the furnace. Prior to heating, a rotary pump lowered the chamber pressure to 10^{-2} torr. At this point, a diffusion pump was activated which further lowered the pressure to 5×10^{-5} torr. The chamber was then backfilled with ultra-high purity N_2 gas passing through a heated iron wool at 750 °C which acted as an O_2 getter. The estimated O_2 in the flow is $\leq$ 0.1 ppm. The temperature was raised at 10 °C / min up to 1100 °C, then immediately cooled to room temperature.

2.2. Scanning/transmission electron microscopy

S/TEM analysis of the CLS samples was performed using an FEI Themis Z C_S probe-corrected S/TEM operated at 200 kV and equipped with a bottom-mounted FEI Ceta 16 M pixel CMOS camera, Fischione Instruments Model 3000 STEM detector, and FEI SuperX SDD energy dispersive spectroscopy (EDS) system. Lamellas for cross-sectional S/TEM analysis of each sample were prepared using FEI Helios Nanolab 600i and FEI Helios G4 PFIB CXe dual focused ion beam/scanning electron microscope systems using *in situ* lift-out methods described elsewhere [25–28]. Prior to lamella preparation, the samples were coated with ~ 100 nm of Cr *via* electron beam-assisted evaporation to reduce charging effects and to provide an initial surface protective layer [29]. The lamellas were plasma cleaned for a few minutes immediately prior to each insertion into the S/TEM to prevent carbonaceous contamination during subsequent analysis [30,31].

Initially, μm-scale bright-field cross-sectional TEM (BF-XTEM) imaging was performed to evaluate the grain structure of the CLS samples followed by μm-scale STEM-EDS mapping to evaluate and quantify the elemental distribution. All reported quantitative EDS results and associated uncertainty were calculated using Cliff-Lorimer analysis[32] in conjunction with the reported performance of the SuperX SDD EDS system [33], calculated ionization cross-sections [34], experimentally measured electron transition probabilities, and experimentally measured fluorescence yields [35].

From each sample, random grains were examined in greater detail by tilting the sample to align a major crystallographic zone axis within each grain with the incident beam direction. Selected area electron diffraction (SAED) was then performed on the grain along with subsequent atomic-resolution high-angle annular dark-field STEM (HAADF-STEM) imaging using a convergence semi-angle of 22 mrad and a probe current of 30 pA.

3. Results

Micro-scale BF-XTEM imaging of the as-synthesized CLS specimen (henceforth called, 'control') is shown in Fig. 1**A**. Four large and well-defined grains can be seen (partially measured as 8.23 μm from end to end). The crystalline quality appears to be high, as is evident from the high angle

grain boundaries separating the grains. The densification appears to be complete with no evidence of porosity. Fig. 1**B** shows μm-scale BF-XTEM imaging of a thermally annealed CLS sample. Clear differences can be observed when compared to the control sample; in fact, three unique microstructures appear to be evident. First, the near-surface region of the sample (up to ~ 2.70 μm in depth) shows presence of sub-micron scale porosity. In the image shown, there are at least 16 pores of varying sizes across the 8.23 μm length of the sample. The largest pore size measured is 0.219 μm. Second, the pores appear to be embedded in a region where the grains recrystallized, as is evidenced by smaller grain sizes in this region, with the average grain size = 0.106 ± 0.048 μm.

Below this near-surface region, a sub-surface region with slightly larger grains with average diameter = 0.284 ± 0.138 μm reside. However, these are much smaller than the large grains found in the bulk of the sample, with average diameter = 3.063 ± 1.651 μm.

To understand the composition of the samples, STEM-EDS elemental mapping (net counts) was conducted on both the control and thermally annealed samples. Here, we focus on the thermally annealed sample to illustrate the key differences in composition observed throughout the cross-section. A comparison of the control CLS and thermally annealed CLS, wide field-of-view, STEM-EDS maps are provided in Supplementary Material S1. The control CLS shows no signs of elemental segregation. In contrast, Fig. 2**A** shows a HAADF-STEM image of the near-surface region of the cross-section. As was the case with the BF-XTEM image shown in Fig. 2**B**, the three unique microstructures are all evident. The elemental maps for calcium (Fig. 2**B**), oxygen (Fig. 2**C**), sulfur (Fig. 2**D**) and lanthanum (Fig. 2**E**) from the same region in Fig. 2**A** are also shown. From these images, it is clear that the surface and sub-surface regions are calcium depleted, while the surface region is oxygen rich. The sulfur

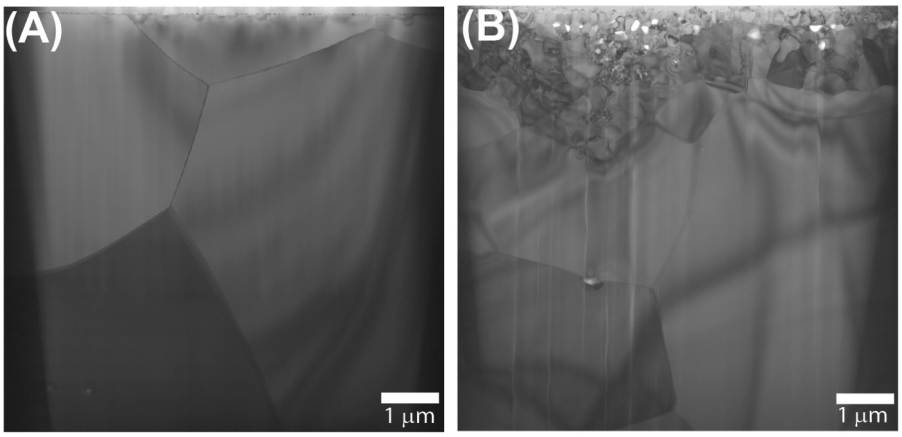

Fig. 1. (A) Cross-section of control CLS sample. (B) Cross-section of thermally annealed CLS sample showing recrystallized grains and sub-micron scale pores near the surface.

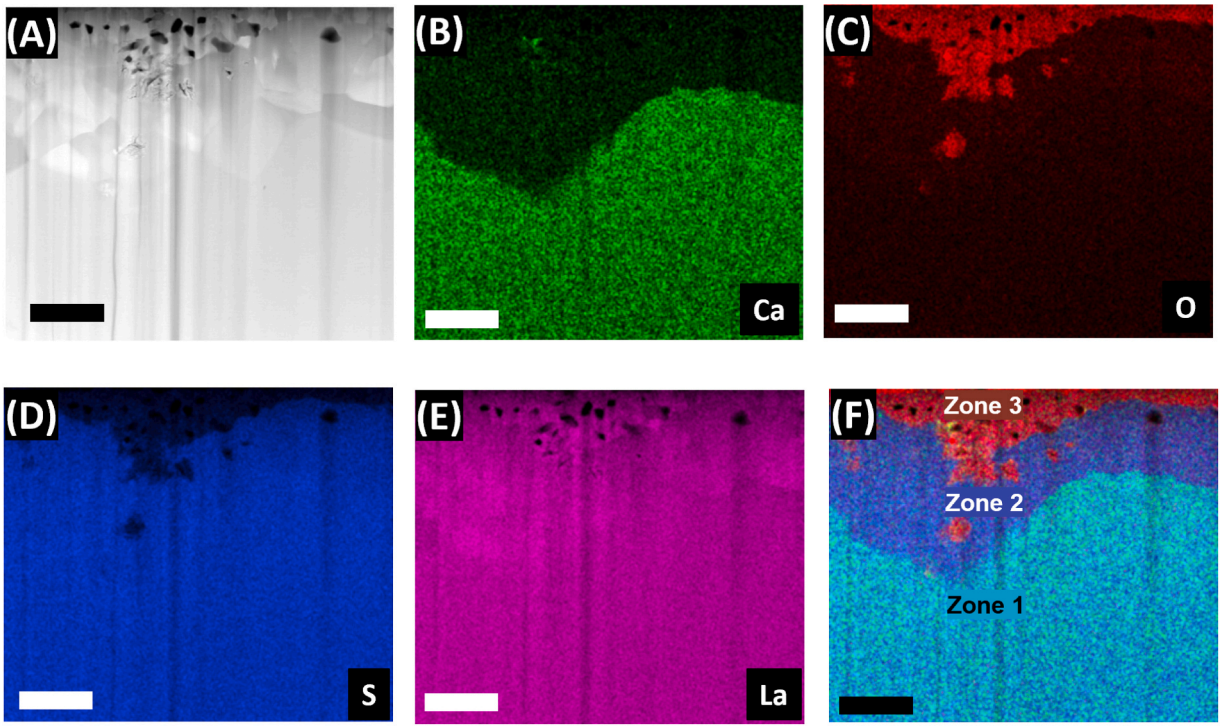

Fig. 2. STEM-EDS elemental maps (net counts) of annealed CLS showing (A) HAADF-STEM image of the mapped area and maps for (B) Ca, (C) O, (D) S, (E) La, and (F) composite color map with Zones 1, 2, and 3 indicated. Note that the contrast limits of each map were set to result in an identical dynamic range; thus, the maps only *qualitatively* indicate where the content of each element is higher or lower. All scale bars: 1 μm.

distribution, while uniform in the sub-surface and bulk regions, is depleted in the surface region. Thus, it appears that sulfur depletion coincides with oxygen enhancement. In contrast to the other three elements, the lanthanum distribution appears to be uniform throughout all three regions.

The composite elemental distribution map with individual elements are overlayed in Fig. 2**F**, which identifies and visually demarcates the different regions (or zones) of the cross-section. We define "Zone 1" as the bulk region where the structural (*i.e.*, related to the well-formed grains and the absence of porosity) and elemental characteristics remain nearly identical to the control CLS sample. This point will be further clarified in subsequent line scans comparing control CLS with the annealed sample. "Zone 2" is the sub-surface region where calcium is depleted while lanthanum and sulfur concentrations remain similar to that of the bulk *i.e.*, Zone 1. Finally, we define "Zone 3" as the near-surface region which is porous and is compositionally oxygen-rich, sulfur-deficient, and calcium-deficient.

To quantitatively understand the composition and stoichiometry of the three zones defined above, we quantified the at% of the individual elements in the control CLS sample versus the thermally annealed CLS sample. These data were obtained from the previous EDS maps and are areal averages over the three zones. Table 1 tabulates the at% for calcium, oxygen, sulfur and lanthanum for the two samples. In the control sample the calcium content is 2.0 ± 0.2 at%. In the thermally annealed sample, Zone 1 exhibits an increased calcium content of 2.4 ± 0.2 at% while Zones 2 and 3 have no detectable calcium content. The oxygen concentration in the control CLS is 5.4 ± 0.5 at%. In the thermally annealed CLS, Zone 1 shows an oxygen content of 3.8 ± 0.3 at%. Subsequently, in Zone 2, the oxygen content increases by a factor of ~ 2× to 7.2 ± 0.6 at% while in Zone 3 the oxygen content increases by a factor of

Table 1
The calculated at% with error of Ca, O, S, and La in control CLS and thermally annealed sample as a function of the three zones, as obtained *via* EDS areal analysis.

	Control (at%)	Thermally annealed		
		Zone 1 (at%)	Zone 2 (at%)	Zone 3 (at%)
Ca	2.0 ± 0.2	2.4 ± 0.2	0.0	0.0
O	5.4 ± 0.5	3.8 ± 0.3	7.2 ± 0.6	38.5 ± 3.2
S	52.6 ± 4.5	53.0 ± 4.5	49.7 ± 4.2	20.3 ± 1.7
La	40.1 ± 3.4	40.8 ± 3.5	43.1 ± 3.7	41.2 ± 3.4

~ 10× to 38.5 ± 3.2 at%. The sulfur content in the control sample is 52.6 ± 4.5 at%, which is similar to the sulfur content of 53.0 ± 4.5 at% in Zone 1 of the thermally annealed sample. In Zone 2, the sulfur content decreases to 49.7 ± 4.2 at%, while in Zone 3, the sulfur content is reduced by a factor of ~ 2.5× to 20.3 ± 1.7 at%. Finally, the lanthanum content in the control CLS sample was 40.1 ± 3.4 at%, while the lanthanum content in all three zones of the thermally annealed sample is at 40.8 ± 3.5, 43.1 ± 3.7, and 41.2 ± 3.4 at% for Zones 1, 2, and 3, respectively.

To further investigate the changes to stoichiometry observed in CLS upon thermal annealing, quantitative elemental profiles (at% versus depth) from 0 (i.e., the surface) to 8.0 μm (i.e., the bulk) were extracted from the previous STEM-EDS maps as shown in Fig. 3. The calcium profile shows that the control CLS maintains a near constant calcium concentration of 2.3 at% across the three zones. On the other hand, the thermally annealed CLS has a similar concentration in the depth range extending from 8.0 to 5.0 μm, coinciding with Zone 1. From 5.0 to 1.7 μm, the calcium content increases and reaches a maximum value of 3.7 at% at a depth of 1.7 μm, which is higher compared to the value of 2.2 at% for the control CLS at the same depth; this depth corresponds to the interface between Zones 2 and 1. At this interface the calcium content is negligible on Zone 2 side and both Zones 2 and 3 are calcium depleted. Additionally, since calcium cannot escape the system *via* the surface, mass conservation demands that calcium must diffuse in the opposite direction, *i.e.*, into the bulk. This accounts for the slightly higher calcium content in Zone 1, specifically near the interface with Zone 2.

The oxygen profile for the control CLS shows an oxygen content of 3.0 at% at a depth of 8.0 μm and gradually rising to 10.0 at% at the surface. For the thermally annealed CLS, the oxygen content at a depth

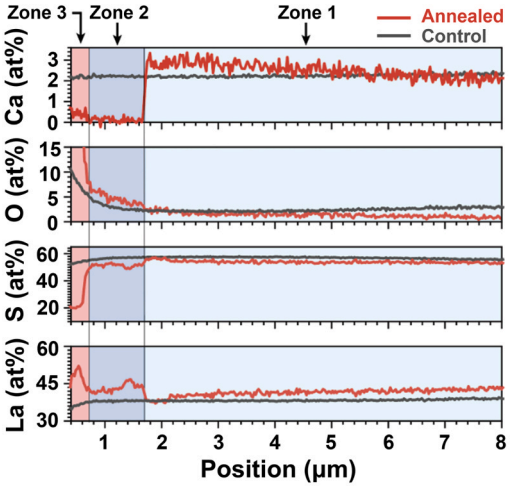

Fig. 3. Quantitative elemental profiles of (from top to bottom) calcium, oxygen, sulfur, and lanthanum as a function of distance from the sample surface (position = 0). The black line profile is from the control sample and the red is from the annealed CLS. The spatial position in depth of zones 1, 2, and 3 are as marked.

of 8.0 μm is ~1.0 at%. At a depth of 2.1 μm, the oxygen content of the thermally annealed CLS starts to increase. For example, at a depth of 0.5 μm the thermally annealed CLS has an oxygen content of 15.0 at% while the content for the control CLS is only at 6.0 at%.

The sulfur profile in the control CLS maintains a relatively constant value of 57.2 at%. throughout the specimen, with a slight drop to 52.6 at % at the surface. On the other hand, the thermally annealed CLS shows a sulfur profile that is 52.6 at% in the bulk (*i.e.*, Zone 1). Approaching the surface through Zone 2 and Zone 3, the thermally annealed CLS has a discontinuous concentration profile dropping to 49.6 at% in Zone 2 and 20.0 at% in Zone 1. The loss in sulfur is expected due to the tendency of sulfur to be lost to ambient during annealing of sulfides [16].

Lastly, the lanthanum profile in the control CLS maintains a constant content of 39.0 at% from 8.0 to 0.5 μm, and thereafter gradually reduces to 34.8 at% approaching the near-surface region. In contrast, the La profile in the thermally annealed CLS shows much more variation. The lanthanum content remains higher than that of the control CLS from 8.0 μm to 2.1 μm, but at 2.1 μm, the content of the thermally annealed sample drops just below that of the control sample until near the Zone 2 interface at a depth of ~1.7 μm. In Zone 2 of the thermally annealed CLS, the lanthanum content is higher compared to the control CLS with the same trend continuing in Zone 3, where a peak lanthanum content of 52.1 at% is observed at a depth of ~ 0.3 μm.

While the spatial variation of elemental composition can be studied both qualitatively and quantitatively with STEM-EDS, it is important to also identify the crystal structure of the phases present. Both stoichiometry and crystal structure provide a complete picture of the transformations induced in CLS during thermal annealing. To this effect, Fig. 4**A** shows the composite STEM-EDS map (net counts) of the thermally annealed CLS sample with the three zones indicated. For individual grains in each zone, atomic-resolution HAADF-STEM imaging and SAED were performed. Fig. 4**B** shows an atomic-resolution HAADF-STEM image within a grain inside Zone 1. The inset shows the SAED pattern of the same region; this is indexed as the Th_3P_4 crystal structure of CLS along the zone axis B = [111] [13,15,21]. Fig. 4**C** shows the atomic-resolution HAADF-STEM image of a grain inside Zone 2. The SAED inset was indexed as the tetragonal $La_{20}OS_{29}$ phase with zone axis B = [201]. It should be noted that prior quantitative EDS results show no evidence of calcium in Zone 2; this is consistent with the crystal structure determined via SAED. Fig. 4**D** shows the atomic-resolution HAADF-STEM image and inset SAED pattern from a grain of Zone 3. The inset SAED pattern was indexed [36,37] as a trigonal La_2O_2S crystal structure with zone axis B = $[10\bar{1}0]$. Similar to Zone 2, it should be noted that prior quantitative EDS results indicated no calcium was present in Zone 3, which is consistent with the crystal structure determined *via* SAED.

4. Discussion

We start the discussion with studying the interrelationships between the three compounds – CLS, $La_{20}OS_{29}$ and La_2O_2S detected in the S/TEM analyses. In order to do this, we present a partial reconstruct of the quaternary phase diagram between calcium, lanthanum, sulfur and oxygen in Fig. 5**A**. This 3D construct is inspired by the phase diagram presented by Chess *et al.* and Kitazawa *et al.*, [8,23] Knowing both the phase diagrams allows us to propose a relationship between the various phases present in thermally annealed CLS. In this figure, the La-O-S system occupies the basal plane, where a tie-line is drawn between La_2S_3 and La_2O_3. Along this line, moving from the sulfur-rich end towards the oxygen-rich end, the following have been reported, i) a solid solution between La_2S_3 and $La_{10}S_{14}O_{1-x}S_x$, x ∈ [0, 1], yielding $La_{20}OS_{29}$ at x = 0.5, and ii) La_2O_2S. Other phases such as $La_2O_2S_2$ do not lie on this tie line and therefore, for clarity are not shown in this Figure. Similarly, the Ca-La-S ternary plane is one of the sides of the pyramid. The tie line of interest on this surface connects the $CaLa_2S_4$ (*i.e.*, the 50:50 CaS:

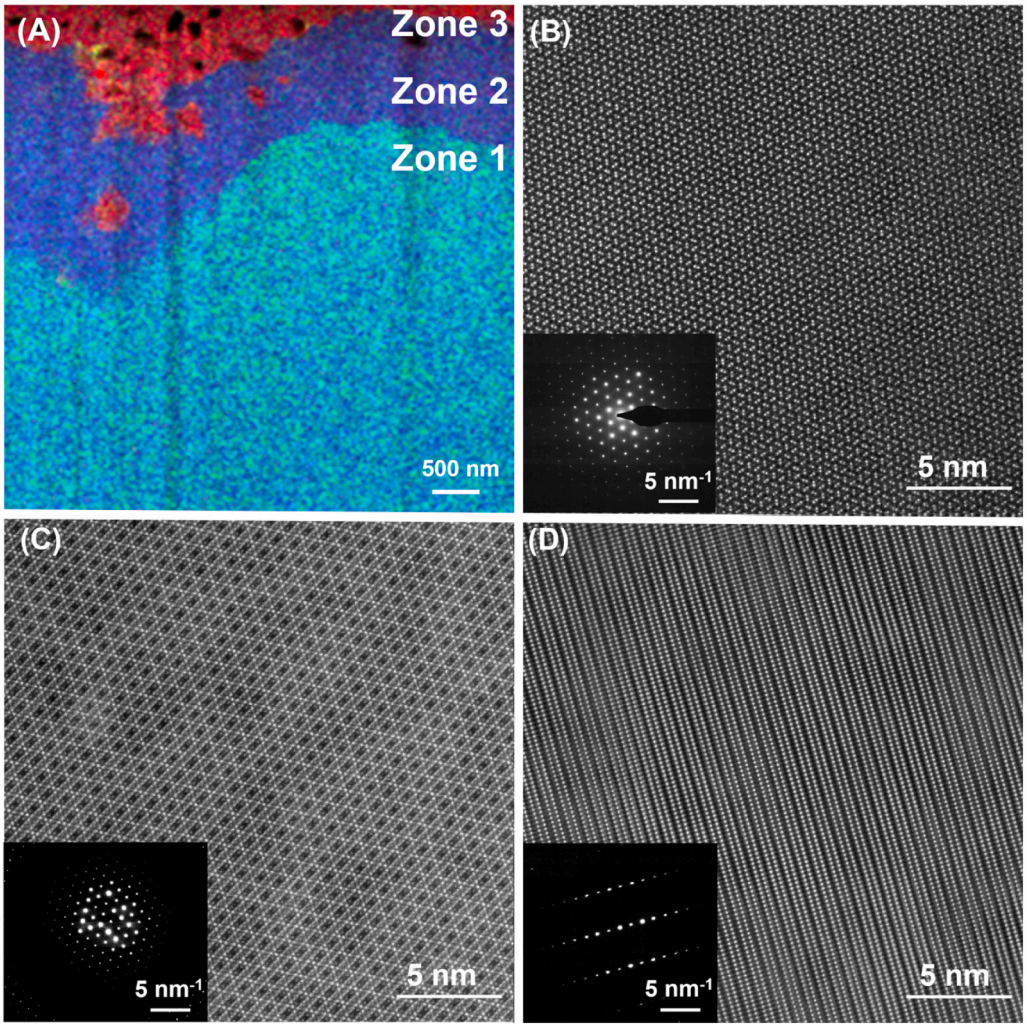

Fig. 4. (A) STEM-EDS composite map of the near-surface region of thermally annealed CLS with the three Zones indicated. (B) Atomic-resolution HAADF-STEM image and SAED (inset) from a grain in Zone 1 corresponding to CLS with cubic Th_3P_4 crystal structure, zone axis B = [111], (C) atomic-resolution HAADF-STEM image and SAED (inset) from a grain in Zone 2 corresponding to the tetragonal phase $La_{20}OS_{29}$ with zone axis B = [201], and (D) atomic-resolution HAADF-STEM image and SAED (inset) from a grain in Zone 3 corresponding to La_2O_2S in the trigonal phase with zone axis B = [10$\bar{1}$0].

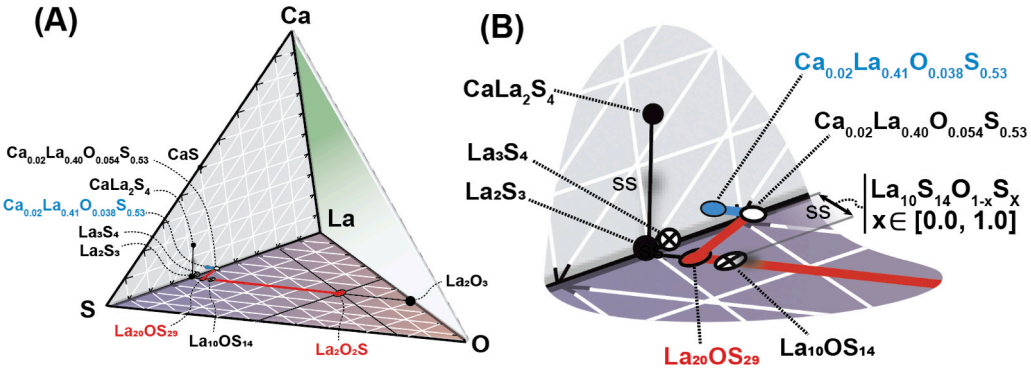

Fig. 5. (A) Partial construct of a quaternary phase diagram for Ca-La-S-O adapted from Kitazawa *et al.*, [23] and Chess *et al.*, [8] showing the CLS solid solution connected *via* a tie line between La_2S_3 and $CaLa_2S_4$ on the Ca – La - S surface. (B) Zoomed up image of region of interest from (A). Potential path in blue, from control CLS open symbol '○' that lies inside the 3D phase diagram due to residual oxygen, to reduced CLS (solid blue), Zone 1. Potential path in red from as-received CLS '○' to Zone 2 ($La_{20}OS_{29}$); and from Zone 2 ($La_{20}OS_{29}$) to Zone 3 (La_2O_2S) lie on the ternary phase space of La-O-S with no Ca. Note: black lines labeled 'ss' = solid solution.

La_2S_3) to La_2S_3 (more specifically, the γ-La_2S_3). On this tie line lie solid solutions between $CaLa_2S_4$ and La_2S_3. For clarity this region of interest is 'zoomed-in' in Fig. 5**B**. All compositions are used from the results of the quantitative EDS analysis with their associated uncertainties.

The starting CLS composition is also labeled as an open circle, $Ca_{0.02}La_{0.40}O_{0.054}S_{0.53}$. Upon thermal annealing, phase decomposition occurs in two directions. The first direction is towards the

Ca-La-S plane and the tie-line (solid solution, 'ss') between $CaLa_2S_4$

and La_2S_3, indicating loss of oxygen. This corresponds to Zone 1 and is shown in Fig. 5**A** and **B** as a blue line. The final composition achieved is $Ca_{0.02}La_{0.41}O_{0.038}S_{0.53}$. A second series of phase decompositions can also be mapped and lies below the starting composition. This phase decomposition is indicated in red and involves two steps. First, a complete loss of calcium which causes the composition to drop onto the La-O-S plane as $La_{20}OS_{29}$ (*i.e.*, Zone 2). This phase lies on a tie-line with solid solution between La_2S_3 and $La_{10}S_{14}O_{1-x}S_x$, $x \in [0,1]$. Second, continued oxygen gain and sulfur loss leads to the formation of La_2O_2S (*i.e.*, Zone 3*)*. The phase decomposition pathways proposed above are consistent with the TEM data that shows the depth-dependent composition and structure observed.

The observation of sub-micron scale porosity in Zone 3 can be explained using two potential mechanisms. First, the generation and trapping of SO_2 gas can lead to formation of pores. However, this mechanism should lead to the formation of pores throughout the bulk and not just in Zone 3. Further, a loss of both S and O should be observed closer to the surface. The elemental line profile of O (Fig. 3) does not support this conclusion. Thus, it appears unlikely that generation of SO_2 is the cause for the observation of sub-micron scale porosity.

A second hypothesis can be proposed by considering the change in molar volumes across the three layers [38]. CaS: La_2S_3 10:90 (at%) (*i.e.,* control CLS in Zone 1) has a theoretical molar volume of 69.8 cm^3/mol (density 4.92 gm/cm^3), $La_{20}OS_{29}$ (*i.e.,* Zone 2) has a theoretical molar volume of 748.6 cm^3/mol (density of 4.97 gm/cm^3) and La_2O_2S (*i.e.,* Zone 3) has a theoretical molar volume of 60.0 cm^3/mol (density of 5.7 gm/cm^3). If the conversion of $La_{20}OS_{29}$ (*i.e.,* Zone 2) to La_2O_2S (*i.e.,* Zone 3) is represented by the following reaction: $La_{20}OS_{29} + 9.5\ O_2 \rightarrow 10La_2O_2S + 19S$, it is seen that 1 mol of $La_{20}OS_{29}$ leads to the formation of 10 moles of La_2O_2S. Thus, the volume change involved is from 748.6 cm^3/ mol to 600 cm^3/mol, which is a loss of 19.8 %. Therefore, to maintain surface coverage, the La_2O_2S layer accommodates the loss in volume by formation of the observed sub-micron scale porosities.

Reaction modeling of the thermal anneal behavior of CLS under low O_2 and low S_2 partial pressures provides an important step in understanding the sequence of processes that lead to the formation of the phases encountered in the S/TEM investigation. This analysis describes *i*) the redox process induced by the evaporative loss of sulfur, *ii*) the diffusive redistribution of atomic species resulting from the formation of sulfur vacancies and *iii*) the formation of secondary phases due to the destabilization of the γ-phase crystal structure. The goal of this modeling exercise is to understand the interdependencies of the phase formation process.

To help us analyze the sequence of processes, we first cast the empirical sum formulae of the *control* and *zone 1* CLS compounds, as obtained by S/TEM analysis, into a Th_3P_4 generic structural formula $[Ca_aLa_bV_c]_3[S_{1-x}O_x]_4$. This formula accounts for the partial substitution of the anion sites by oxygen and the partial reduction of the CLS compound due to sulfur loss. Further, to help balance the redox equations any excess negative charge resulting from the oxidation of sulfur upon volatilization is assumed to delocalize, resulting in *n*-type semiconducting CLS. The volatilization reaction of sulfur from CLS into mostly diatomic sulfur [39] in Kröger-Vink notation is given as:

$$2S_S^X \rightarrow 2V_S^{\bullet\bullet} + 4e^- + S_2(g)\uparrow \quad (1)$$

The structural formula $[Ca_aLa_bV_c]_3[S_{1-x}O_x]_4$ assumes that the anion sublattice is filled, while the cation sublattice may support structural vacancies 'V'.

All coefficients *a, b, c* and *x* satisfy:

$$(a,b,c,x) \in [0,1] \text{and} a+b+c=1 \quad (2)$$

with the additional constraint that, the anion-to-cation ratio in CLS solid-solutions must range between 4/3 and 3/2 to be stable, that is:

$$\frac{4}{3} \le \frac{4}{3(a+b)} \le \frac{3}{2} \quad (3)$$

i.e.,

$$\frac{8}{9} \le a+b \le 1 \quad (4)$$

And therefore by virtue of Eq. 2,

$$0 \le c \le \frac{1}{9} \quad (5)$$

Hence, accounting for the experimental quantification uncertainties, it can be shown that using elemental, charge and site conservation laws, the stoichiometry of the control CLS can be written as:

$$Ca_{0.020}La_{0.401}O_{0.054}S_{0.525} \sim 0.146 \bullet [Ca_{0.046}La_{0.915}V_{0.039}]_3[S_{0.908}O_{0.092}]_4$$

whereas the CLS of *zone 1* is:

$$Ca_{0.024}La_{0.408}O_{0.038}S_{0.530} \sim 0.142 \bullet [Ca_{0.056}La_{0.944}V_{0.0}]_3[S_{0.933}O_{0.067}]_4$$

The former formula shows that the control CLS is already partially reduced (n-type and sub-stoichiometric CLS) and that the anion sublattice is filled. The latter formula reveals that structural cation vacancies are no longer present in Zone 1 CLS and have been depleted by the anion vacancies created by the evaporative loss of sulfur through an anti-Schottky annihilation process. Finally, the decomposition of CLS during thermal annealing can be written as:

$$[Ca_{0.046}La_{0.915}V_{0.039}]_3[S_{0.908}O_{0.092}]_4 \rightarrow 0.821 \bullet [Ca_{0.056}La_{0.944}V_{0.0}]_3[S_{0.933}O_{0.067}]_4 + 0.042 \bullet S_2(g)\uparrow + 0.067 \bullet La_2O_2S + 0.014 \bullet La_{20}OS_{29} \quad (6)$$

Fig. 6 proposes snapshots of a possible time-sequence for this redox reaction. The process starts with an O-doped lanthanum-rich CLS base material with a cubic Th_3P_4 crystalline structure and structural cation vacancies (blue squares). During annealing under low p_{S2}, negatively charged anion vacancies (red squares) form in the sub-surface due to sulfur evaporation. Cation and anion vacancies annihilate in the sub-surface yielding n-type CLS with filled cation and anion sublattices. If further sulfur evaporates, the newly formed anion vacancies can no longer annihilate as in step '3' and diffuse deeper into the solid. These vacancies create an anion-to-cation ratio imbalance that destabilizes the Th_3P_4 structure. Assuming that the fluxes of oxygen and sulfur ions are such that $j_{O2-} >> j_{S2-}$ and that lanthanum ions are more mobile than calcium ions, $j_{La3+} >> j_{Ca2+}$, the flux of vacancies sets about an opposite flux of oxygen ions charge-compensated by a flux of lanthanum that results in the formation of an oxysulfide layer at the surface of the sample. As stated before, the release of sulfur and changes to molar volume as a result of the formation of La_2O_2S layer on $La_{20}OS_{29}$ produces sub-micron scale porosity in Zone 3.

5. Conclusion

Using S/TEM, we have established structure – phase – composition relationships between the base ceramic and the two oxysulfide phases formed as a result of thermal annealing at 1100 °C in an inert N_2 environment. The starting CLS was a lanthanum-rich CaS: La_2S_3 of 10: 90 at % composition. The sample was characterized by large and well-developed grains and no observable porosity. While theoretically, the Ca: La: S at% was expected to be 2.1: 38.3: 59.6, the measured composition of the control sample with the addition of residual oxygen was Ca: La: S: O with 2.0: 40.1: 52.5: 5.4 at%.

S/TEM analyses of a cross-section of the annealed CLS sample showed the presence of three zones. The deepest zone (Zone 1) extended beyond 1.7 μm under the surface and showed the cubic Th_3P_4 crystal structure with similar grain morphology as the control sample.

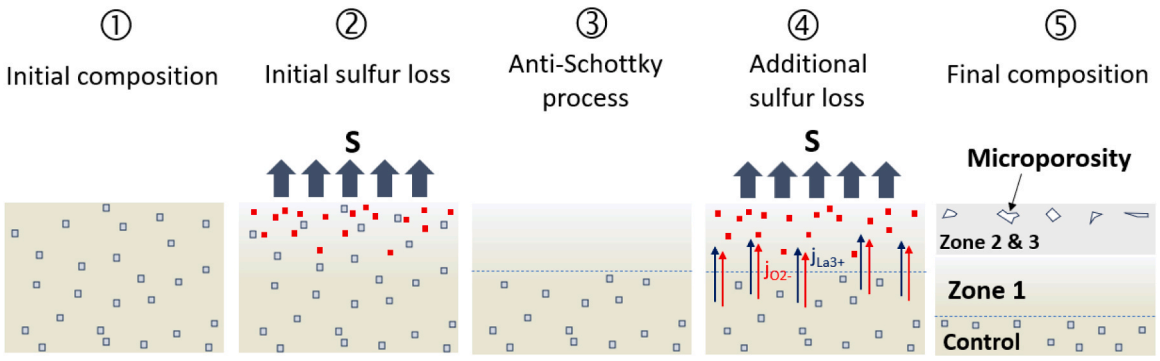

Fig. 6. Proposed sequence of processes leading up to the phase transformation observed during thermal annealing of lanthanum-rich CLS with dissolved O in a low sulfur partial pressure atmosphere. Blue and red squares represent structural cation vacancies and anion vacancies, respectively. See text for details.

Compared to the control sample, this zone showed a slightly higher calcium content and slightly lower oxygen content. In the intermediate zone (Zone 2) small, recrystallized grains were observed extending from a depth of 0.7 μm to 1.7 μm below the surface. The oxygen content monotonically increased moving closer to the surface and reached a maximum content of 7.2 at%. This zone was completely depleted of calcium. SAED showed that the phase of the recrystallized grains in this zone was tetragonal $La_{20}OS_{29}$. Finally, the zone closest to the surface (Zone 3) showed sub-micron scale porosity and recrystallized grains with an excessively high oxygen content of 38.5 at%, depleted sulfur content of 20.3 at% and negligible calcium content. The phase in this zone was identified as trigonal La_2O_2S.

Thus, thermal annealing of lanthanum-rich CLS in an inert atmosphere causes the formation of a sequence of layered phases of varying composition. The excess oxygen and loss in calcium in the near-surface region causes the decomposition of CLS into a series of calcium-free, oxysulfide phases of increasing O content, sequentially formed near the surface. These results can be explained within a framework of established phase diagrams of La-O-S and CaS – La_2S_3 and defect reactions of the various elemental species during the phase transformation process.

CRediT authorship contribution statement

Kathleen A Richardson: Writing – review & editing, Supervision, Software, Resources, Project administration, Funding acquisition, Conceptualization. **Andrew Cooper:** Writing – review & editing, Visualization, Formal analysis, Data curation. **Brian Butkus:** Writing – review & editing, Visualization, Formal analysis, Data curation. **Andrew Howe:** Writing – review & editing, Investigation, Data curation, Conceptualization. **Parag Banerjee:** Writing – review & editing, Writing – original draft, Visualization, Supervision, Resources, Project administration, Investigation, Funding acquisition, Formal analysis, Data curation. **Romain Gaume:** Writing – review & editing, Writing – original draft, Visualization, Validation, Supervision, Software, Resources, Project administration, Funding acquisition, Formal analysis, Data curation, Conceptualization. **Nicholas G Rudawski:** Writing – review & editing, Visualization, Validation, Software, Methodology, Investigation, Formal analysis, Data curation. **Alexandros Kostogiannes:** Visualization, Validation, Methodology, Investigation, Formal analysis, Data curation, Conceptualization. **Brianna Ellsworth:** Writing – original draft, Visualization, Investigation.

Declaration of Competing Interest

The authors declare that they have no known competing financial interests or personal relationships that could have influenced the work reported in this paper.

Acknowledgments

The authors acknowledge Lockheed Martin Corporation for support of this work and to Dr. Clara Rivero-Baleine for helpful discussions. BE thanks the support of UCF's College of Engineering and Computer Science Dean's graduate fellowship. This work was supported in part by the NSF I/UCRC on Multi-functional Integrated System Technology (MIST) Center, award number 1939050. The Herbert Wertheim College of Engineering Research Service Centers at the University of Florida is acknowledged for use of the dual FIB/SEM and S/TEM instrumentation.

Appendix A. Supporting information

Supplementary data associated with this article can be found in the online version at doi:10.1016/j.jeurceramsoc.2024.117062.

References

[1] K.J. Saunders, T.Y. Wong, R.L. Gentilman, Optical, mechanical and thermal properties of $CaLa_2S_4$, Proc. SPIE (1984) 31–34.
[2] K. Saunders, T. Wong, T. Hartnett, R. Tustison, R. Gentilman, Current and Future Development of Calcium Lanthanum Sulfide. Proc SPIE, SPIE, 1986, pp. 72–78.
[3] J. Covino, D.C. Harris, M.E. Hills, R.T. Loda, R.W. Schwartz, Development of calcium lanthanum sulfide as an 8-12 micrometer transmitting ceramic, Proc. SPIE (1984) 42–46.
[4] O. Merdrignac-Conanec, G. Durand, S. Walfort, N. Hakmeh, X.H. Zhang, Elaboration of $CaLa_2S_4$ transparent ceramics from novel precursor powders route, Ceram. Int. 43 (8) (2017) 5984–5989.
[5] G. Durand, Élaboration de céramiques transparentes de $CaLa_2S_4$ pour applications optiques dans l'infrarouge, University of Rennes, Francais, 2017, p. 203.
[6] J. Savage, K. Marsh, A materials study to find an advanced optical window material for 8 to 12 μm airborne applications. Proc SPIE, SPIE, 1982, pp. 35–37.
[7] J.A. Beswick, D.J. Pedder, J.C. Lewis, F.W. Ainger, New infra-red window materials, Proc. SPIE (1983) 12–20.
[8] D.L. Chess, C.A. Chess, J.A. Marks, W.B. White, Phase equilibria and processing of infrared optical ceramics on the join CaLa2S4-La2S3, J. Ceram. Process. Res. 11 (4) (2010) 465–470.
[9] J. Flahaut, L. Domange, M. Patrie, A.-M. Bostsarron, M. Guittard, Nonstoichiometric phases in the MS-M_2S_3 sulfide systems. Nonstoichiometric Compounds, American Chemical Society, 1963, pp. 179–190.
[10] J. Flahaut, M. Guittard, M. Patrie, M. Pardo, S. Golabi, L. Domange, Phase cubiques type Th_3P_4 dans les sulfures, les séléniures et les tellurures L_2X_3 et L_3X_4 des terres rares, et dans leurs combinaisons ML_2X_4 avec les sulfures et séléniures MX de calcium, strontium et baryum. Formation et propriétés cristallines, Acta Crystallogr 19 (1) (1965) 14–19.
[11] W.H. Zachariasen, Crystal chemical studies of the 5f-series of elements. VI. The Ce_2S_3–Ce_3S_4 type of structure, Acta Crystallogr 2 (1) (1949) 57–60.
[12] E.D. Eastman, L. Brewer, L.A. Bromley, P.W. Gilles, N.L. Lofgren, Preparation and properties of refractory cerium sulfides, J. Am. Chem. Soc. 72 (5) (1950) 2248–2250.
[13] M. Havel, A. Kostogiannes, W.T. Shoulders, V. Blair, D. McGill, C. Rivero-Baleine, R. Bunijevac, J. Eichler, M.R. Kincer, M. Kang, Monitoring sulfur loss in polycrystalline solid solutions of CaS-La_2S_3 by Raman spectroscopy and X-ray diffraction, Opt. Mater. Express 13 (2) (2023) 504–513.
[14] P. Besançon, Teneur en oxygéne et formule exacte d'une famille de composés habituellement appelés "variété β" ou "phase complexe" des sulfures de terres rares, J. Solid State Chem. 7 (2) (1973) 232–240.
[15] C.M. Vaughan, W.B. White, Role of oxygen in rare earth chalcogenide semiconductors, MRS Proc. (1987) 397–402.

[16] M.S. Tsai, M.H. Hon, Hot-press sintering and the properties of lanthanum-rich calcium lanthanum sulfide ceramic, J. Mater. Res. 9 (11) (1994) 2939–2943.
[17] K.J. Saunders, T.Y. Wong, R.L. Gentilman, Optical, mechanical and thermal properties of $CaLa_2S_4$. Advances in Optical Materials, SPIE, 1984, pp. 31–34.
[18] C. Lowe-Ma, Characterization of rare earth sulfides, in: D.R. Rossington, R. A. Condrate, R.L. Snyder (Eds.), Advances in Materials Characterization, Springer US, Boston, MA, 1983, pp. 267–279.
[19] B.J. Tsay, L.H. Wang, M.H. Hon, The infrared transmission of $Pb_{0.1}Ca_{0.9}La_2S_4$ pellets in the 2.5-14 μm region, Jpn. J. Appl. Phys. 37 (12A) (1998) 6414–6417.
[20] L.H. Wang, M.H. Hon, Infrared transmission curves of $Pb_{0.1}Ca_{0.9}La_2S_4$ pellets densified by pressureless sintering, Mater. Manuf. Process. 14 (5) (1999) 741–753.
[21] B.J. Tsay, L.H. Wang, M.H. Hon, Formation and densification of CaLa2S4 powders by sulfidization of modified metal alkoxides in different atmospheres, Mater. Sci. Eng., B 72 (2000) 31–35.
[22] G.R. Durand, Q. Bizot, N. Herbert, S. Quéméré, M. Pasturel, X.H. Zhang, O. Merdrignac-Conanec, Processing of CaLa2S4 infrared transparent ceramics: A comparative study of HP and FAST/SPS techniques, J. Am. Ceram. Soc. 103 (4) (2019) 2328–2339.
[23] Y. Kitazawa, Y. Kunimoto, M. Wakihara, M. Taniguchi, Phase equilibria and oxidation mechanisms in the La-SO system, J. Therm. Anal. Calor. 25 (2) (1982) 279–290.
[24] A. Kostogiannes, B. Butkus, A. Howe, B. Ellsworth, A. Cooper, P. Banerjee, R. Gaume, K.A. Richardson, Evidence for Substitutional Oxygen in γ – Calcium Lanthanum Sulfide, Submitted.
[25] L.A. Giannuzzi, J.L. Drown, S.R. Brown, R.B. Irwin, F.A. Stevie, Applications of the FIB lift-out technique for TEM specimen preparation, Microsc. Res. Tech. 41 (4) (1998) 285–290.
[26] L.A. Giannuzzi, F.A. Stevie, A review of focused ion beam milling techniques for TEM specimen preparation, Micron 30 (3) (1999) 197–204.
[27] J. Mayer, L.A. Giannuzzi, T. Kamino, J. Michael, TEM sample preparation and FIB-induced damage, MRS Bull. 32 (5) (2007) 400–407.
[28] M. Schaffer, B. Schaffer, Q. Ramasse, Sample preparation for atomic-resolution STEM at low voltages by FIB, Ultramicroscopy 114 (2012) 62–71.
[29] B.W. Kempshall, L.A. Giannuzzi, B.I. Prenitzer, F.A. Stevie, S.X. Da, Comparative evaluation of protective coatings and focused ion beam chemical vapor deposition processes, J. Vac. Sci. Technol. B 20 (1) (2002) 286–290.
[30] T.C. Isabell, P.E. Fischione, Applications of plasma cleaning for electron microscopy of semiconducting materials, MRS Proc. (1998) 31–38.
[31] T.C. Isabell, P.E. Fischione, C. O'Keefe, M.U. Guruz, V.P. Dravid, Plasma Cleaning and Its Applications for Electron Microscopy, Microsc. Microanal. 5 (2) (2002) 126–135.
[32] G. Cliff, G.W. Lorimer, The quantitative analysis of thin specimens, J. Microsc. 103 (2) (1975) 203–207.
[33] P. Schlossmacher, D. Klenov, B. Freitag, H. von Harrach, Enhanced detection sensitivity with a new windowless XEDS system for AEM based on silicon drift detector technology, Microsc. Today 18 (4) (2010) 14–20.
[34] X. Llovet, C.J. Powell, F. Salvat, A. Jablonski, Cross sections for inner-shell ionization by electron Impact, J. Phys. Chem. Ref. Data 43 (1) (2014).
[35] K. Meddouh, S. Daoudi, A. Kahoul, J.M. Sampaio, J.P. Marques, F. Parente, N. K. Aylikci, V. Aylikci, Y. Kasri, A. Hamidani, Average K-, L-, and M-shell fluorescence yields: a new semi-empirical formulae, Radiat. Phys. Chem. 202 (2023) 110481.
[36] W.H. Zachariasen, Crystal chemical studies of the 5f-series of elements. VII. The crystal structure of Ce_2O_2S, La_2O_2S and Pu_2O_2S, Acta Crystallogr 2 (1) (1949) 60–62.
[37] B. Morosin, D.J. Newman, La_2O_2S structure refinement and crystal field, Acta Crystallogr B 29 (11) (1973) 2647–2648.
[38] A. Jain, S.P. Ong, G. Hautier, W. Chen, W.D. Richards, S. Dacek, S. Cholia, D. Gunter, D. Skinner, G. Ceder, K.A. Persson, Commentary: the materials project: a materials genome approach to accelerating materials innovation, APL Mater. 1 (1) (2013).
[39] V.E. Kaloidas, N.G. Papayannakos, Hydrogen production from the decomposition of hydrogen sulphide. Equilibrium studies on the system H2S/ H2/Si, (i = 1,…,8) in the gas phase, Int. J. Hydrog. Energy 12 (6) (1987) 403–409.